Chirality-selective superfluorescence based on chiral interactions

Hirofumi Shiraki,[1] Nobuhiko Yokoshi,[2] and Hajime Ishihara[3,4,*]

[1]*Department of Physics and Electronics, Osaka Prefecture University, 1-1 Naka-ku, Sakai, Osaka 599-8531, Japan*

[2]*Department of Physics and Electronics, Osaka Metropolitan University, 1-1 Naka-ku, Sakai, Osaka 599-8531, Japan*

[3]*Department of Material Engineering Science, Graduate School of Engineering Science, Osaka University, 1-3 Machikaneyama, Toyonaka, Osaka 560-8531, Japan*

[4]*Center for Quantum Information and Quantum Biology, Osaka University, 1-3 Machikaneyama, Toyonaka, Osaka 560-8531, Japan*

(Received 11 April 2022; revised 17 September 2022; accepted 1 November 2022; published 14 November 2022)

The concept of chiral interactions has been intensively studied in various fields involving diverse scales of objects, e.g., nucleons, amino acids, and liquid crystals. One of the key problems is how chiral interactions induce synchronization effects among initially uncorrelated objects. In this study, we propose a model of chirality-selective synchronized fluorescence (superfluorescence) that involves spirally configured quantum emitters at the center of a spirally stacked metal nanostructure. The emitters mutually develop the correlation in time by repeatedly exchanging the radiated photons, which experience the chirality of their environment. We numerically show that the peak fluorescent intensity strongly depends on whether or not the chiralities of the emitters and the metals match, even though the localized surface plasmon decays sufficiently at the positions of the emitters. Our model of chirality-selective superfluorescence will provide an alternative tool for analyzing chiral interactions in synchronization processes.

DOI: 10.1103/PhysRevA.106.053511

I. INTRODUCTION

Chirality is a geometrical property of structures and phenomena that is defined as the absence of mirror symmetry [1,2]. Various phenomena to which chirality applies are known in a wide variety of fields, such as chemistry, material physics, optics, and biology [3–5]. In particular, the interplay between chiral objects and light or electron spin is notable because it produces remarkable physical and chemical phenomena. For example, the processes by which the circular dichroism (CD) of single molecules can be magnified is an important topic in biology and analytical chemistry.

Recently, there have been many fascinating reports on chiral interactions. For example, localized surface plasmon resonance in nearby chiral metallic structures significantly enhances molecular CD, wherein the interaction between the induced polarizations of chiral molecules and the "superchiral field" plays a significant role [6–13]. References [14–16] reported that chiral light beams with orbital angular momentum create chiral structures on metallic and polymer surfaces via mass transport. In addition, electrons that pass through chiral molecules such as DNA exhibit large spin polarizations [17–20]. In Ref. [21], it was reported that the plasmonic chiral field strongly affects the chiral crystallization of achiral molecules, which could control the enantiomeric excess ratio through the enhanced chiral field. Although the basic mechanism underlying these chiral interactions is not fully understood, the dynamics that result from the interplay between the chiral environment and chiral objects is an important issue in many scientific fields.

In this study, we consider the problem of how interparticle correlations and synchronizations are affected by chiral environments. Synchronization was first studied by Huygens based on the motion of two pendulum clocks [22], wherein the two pendulums coordinate their motions in union. The synchronization between objects occurs through various mechanisms, such as molecular-molecular interactions, hydrodynamic effects of solvents, and emitted light fields. Such synchronization should reflect the nature of the immediate environment. As mentioned above, chiral environments play significant roles in various physical and chemical processes. In this study, we propose a model of a system that intelligibly expresses the interplay between the chiral environment and the cooperative phenomena within it. To use an example of typical chiral cooperative effects, we focus on a phenomenon called "superfluorescence" [23,24]. Superfluorescence is a form of cooperative photoluminescence from quantum emitters that occurs through multiple exchanges of emitted photons. Superfluorescence has been studied for many years since Dicke's study, and many interesting studies on it have been reported [25–33]. As an explicit model, let us consider spirally configured emitters with right-handed and left-handed chiralities. If we combine them with right- and left-handed spirally arranged metallic structures, two cases arise: (i) the chirality of the emitter configuration and that of the metallic structures match (the parallel combination) or (ii) they are opposites (the antiparallel combination). If the chiral interactions between the emitters and the environment affect the development of the interemitter correlations, the synchronized fluorescence is expected to be different for different

*ishi@mp.es.osaka-u.ac.jp

combinations. However, in investigating the effect of chiral interactions, there are other factors that can possibly affect the abovementioned difference. For example, if the emitters encounter differently enhancements in the plasmonic fields between the parallel and antiparallel combinations, or if the fabricated samples have any fluctuations in terms of size or position of building blocks (see Fig. 10 in Appendix C), the effect of the chirality may be masked, which increases the difficultly in identifying pure chiral environment effects in the observed difference, even if they are strong. Therefore, in this study, we propose the design of "ideal models" to theoretically investigate the effects originating purely from chirality, which aids in revealing the essences of chiral interactions in chiral environments that would appear in actual experiments. By using such a model, we study how the plasmonic boosting of superfluorescence is selectively activated according to whether the combination is parallel or antiparallel.

II. THEORETICAL METHOD AND MODEL

First, we describe our theoretical method. For the calculations of superfluorescence in the dispersed two-level particle systems (emitters), we start with the Hamiltonian [34], which is expressed as

$$\hat{H} = \sum_{i}^{N} \hbar\omega_i \sigma_{10}^{i}\sigma_{01}^{i} + \sum_{\lambda}\int d\boldsymbol{k}\hbar\omega_{\boldsymbol{k}} b_{\boldsymbol{k}\lambda}^{\dagger} b_{\boldsymbol{k}\lambda} - \int d\boldsymbol{r}\sum_{i}^{N} \hat{\boldsymbol{d}}_i \cdot \hat{\boldsymbol{E}}(\boldsymbol{r}), \tag{1}$$

where σ_{10}^{i} and σ_{01}^{i} represent the ladder operators of the ith emitter modeled by a two-level system; $b_{\boldsymbol{k}\lambda}$ and $b_{\boldsymbol{k}\lambda}^{\dagger}$ represent the creation and annihilation operators of the photon, respectively; λ is the index of the polarization direction; $\boldsymbol{k}$ is the wave number; $\hbar\omega_i$ and $\hbar\omega_{\boldsymbol{k}}$ are the energies of the two-level particle at $\boldsymbol{r} = \boldsymbol{r}_i$ and the photon, respectively; and $\hat{\boldsymbol{d}}_i$ and $\hat{\boldsymbol{E}}$ are the operators of the dipole moment of the ith emitter and the electric field, respectively. The latter two variables are expressed by

$$\hat{\boldsymbol{d}}_i = \left(\sigma_{01}^{i} + \sigma_{10}^{i}\right)\boldsymbol{d}_i\delta(\boldsymbol{r} - \boldsymbol{r}_i), \tag{2}$$

$$\hat{\boldsymbol{E}}(\boldsymbol{r}) = i\sum_{\lambda}\int d\boldsymbol{k}\sqrt{\frac{\hbar\omega_{\boldsymbol{k}}}{16\pi^3\epsilon_0}}\left[b_{\boldsymbol{k}\lambda}\boldsymbol{f}_{\boldsymbol{k}\lambda}(\boldsymbol{r}) - b_{\boldsymbol{k}\lambda}^{\dagger}\boldsymbol{f}_{\boldsymbol{k}\lambda}^{*}(\boldsymbol{r})\right], \tag{3}$$

where $\boldsymbol{d}_i$ is the matrix of the transition dipole moment of the ith emitter, ϵ_0 is the vacuum permittivity, and $\boldsymbol{f}_{\boldsymbol{k}\lambda}(\boldsymbol{r})$ is an eigenfunction satisfying Maxwell's equations and is expressed as

$$\nabla \times \nabla \times \boldsymbol{f}_{\boldsymbol{k}\lambda}(\boldsymbol{r}) - \epsilon(\boldsymbol{r})\left(\frac{\omega_{\boldsymbol{k}}}{c}\right)^2 \boldsymbol{f}_{\boldsymbol{k}\lambda}(\boldsymbol{r}) = 0, \tag{4}$$

where $\epsilon(\boldsymbol{r})$ is the dielectric constant of the medium at $\boldsymbol{r}$. Hence, $\boldsymbol{f}_{\boldsymbol{k}\lambda}(\boldsymbol{r})$ can be defined even for inhomogeneous media.

Next, we simultaneously solve the Heisenberg equations for the following elements: the photon density $\langle b_{\boldsymbol{k}\lambda}^{\dagger} b_{\boldsymbol{k}\lambda}\rangle$, the photon-assisted polarization $\langle b_{\boldsymbol{k}\lambda}^{\dagger}\sigma_{01}^{i}\rangle$, the excited-state occupation $\langle\sigma_{10}^{i}\sigma_{01}^{i}\rangle$, and the correlation between emitters $\langle\sigma_{10}^{i}\sigma_{01}^{j}\rangle$. We apply the adiabatic approximation to the simultaneous equations. When the formation of polarization is faster than other timescales, this approximation can be integrated in typical exitonic systems. The validity for this approximation is discussed in the previous studies [34,35]. Based on these factors, the time derivative of $\langle b_{\boldsymbol{k}\lambda}^{\dagger}\sigma_{01}^{i}\rangle$ becomes zero, and we obtain the following stationary solution:

$$\langle b_{\boldsymbol{k}\lambda}^{\dagger}\sigma_{01}^{i}\rangle = \frac{i}{\omega_{\boldsymbol{k}} - \omega_i}\sqrt{\frac{\omega_{\boldsymbol{k}}}{16\pi^3\epsilon_0\hbar}}\left(\boldsymbol{d}_i \cdot \boldsymbol{f}_{\boldsymbol{k}\lambda}(\boldsymbol{r}_i)\langle\sigma_{10}^{i}\sigma_{01}^{i}\rangle + \sum_{m\neq i}^{N}\boldsymbol{d}_m \cdot \boldsymbol{f}_{\boldsymbol{k}\lambda}(\boldsymbol{r}_m)\langle\sigma_{10}^{m}\sigma_{01}^{i}\rangle\right). \tag{5}$$

In addition, to describe the photon field, we define a dyadic Green's function as

$$\boldsymbol{G}(\boldsymbol{r}, \boldsymbol{r}', \omega) = \sum_{\lambda}\int d\boldsymbol{k}\frac{\omega_{\boldsymbol{k}}\boldsymbol{f}_{\boldsymbol{k}\lambda}^{*}(\boldsymbol{r}')\boldsymbol{f}_{\boldsymbol{k}\lambda}(\boldsymbol{r})}{16\pi^3(\omega_{\boldsymbol{k}} - \omega)}. \tag{6}$$

By combining Eqs. (5) and (6), we can describe $\langle\sigma_{10}^{i}\sigma_{01}^{i}\rangle$ and $\langle\sigma_{10}^{i}\sigma_{01}^{j}\rangle$ by

$$\frac{\partial}{\partial t}\langle\sigma_{10}^{i}\sigma_{01}^{i}\rangle = \frac{2}{\hbar\epsilon_0}\mathrm{Im}\left[\boldsymbol{d}_i \cdot \boldsymbol{G}^{*}(\boldsymbol{r}_i, \boldsymbol{r}_i, \omega_i) \cdot \boldsymbol{d}_i\langle\sigma_{10}^{i}\sigma_{01}^{i}\rangle\right] + \frac{2}{\hbar\epsilon_0}\sum_{j\neq i}^{N}\mathrm{Im}\left[\boldsymbol{d}_j \cdot \boldsymbol{G}^{*}(\boldsymbol{r}_j, \boldsymbol{r}_i, \omega_i) \cdot \boldsymbol{d}_i\langle\sigma_{10}^{j}\sigma_{01}^{i}\rangle\right], \tag{7}$$

$$\begin{aligned}\frac{\partial}{\partial t}\langle\sigma_{10}^{i}\sigma_{01}^{j}\rangle &= i(\omega_i - \omega_j)\langle\sigma_{10}^{i}\sigma_{01}^{j}\rangle \\ &- \frac{i}{\hbar\epsilon_0}\left(1 - 2\langle\sigma_{10}^{i}\sigma_{01}^{i}\rangle\right)\boldsymbol{d}_j \cdot \boldsymbol{G}^{*}(\boldsymbol{r}_j, \boldsymbol{r}_i, \omega_j) \cdot \boldsymbol{d}_i\langle\sigma_{10}^{j}\sigma_{01}^{j}\rangle - \frac{i}{\hbar\epsilon_0}\left(1 - 2\langle\sigma_{10}^{i}\sigma_{01}^{i}\rangle\right)\sum_{m\neq j}^{N}\boldsymbol{d}_m \cdot \boldsymbol{G}^{*}(\boldsymbol{r}_m, \boldsymbol{r}_i, \omega_j) \cdot \boldsymbol{d}_i\langle\sigma_{10}^{m}\sigma_{01}^{j}\rangle \\ &+ \frac{i}{\hbar\epsilon_0}\left(1 - 2\langle\sigma_{10}^{j}\sigma_{01}^{j}\rangle\right)\boldsymbol{d}_i \cdot \boldsymbol{G}(\boldsymbol{r}_i, \boldsymbol{r}_j, \omega_i) \cdot \boldsymbol{d}_j\langle\sigma_{10}^{i}\sigma_{01}^{i}\rangle \\ &+ \frac{i}{\hbar\epsilon_0}\left(1 - 2\langle\sigma_{10}^{j}\sigma_{01}^{j}\rangle\right)\sum_{m\neq i}^{N}\boldsymbol{d}_m \cdot \boldsymbol{G}(\boldsymbol{r}_m, \boldsymbol{r}_j, \omega_i) \cdot \boldsymbol{d}_j\langle\sigma_{10}^{i}\sigma_{01}^{m}\rangle.\end{aligned} \tag{8}$$

Here, we have approximately factorized the correlation functions, e.g., $\langle\sigma^i_{10}\sigma^i_{01}\sigma^i_{10}\sigma^j_{01}\rangle \simeq \langle\sigma^i_{10}\sigma^i_{01}\rangle\langle\sigma^i_{10}\sigma^j_{01}\rangle$. We can solve this set of simultaneous equations [Eqs. (7) and (8)] using the Runge-Kutta method. To visualize the dynamics of superfluorescence, we calculate the emission intensity $n_p(t)$ using the time derivative of the photon density. By using $\langle\sigma^i_{10}\sigma^i_{01}\rangle$ and $\langle\sigma^i_{10}\sigma^j_{01}\rangle$ obtained from Eqs. (7) and (8), we can calculate the emission intensity as follows:

$$\begin{aligned} n_p(t) &= \sum_\lambda \int d\boldsymbol{k} \frac{\partial}{\partial t}\langle b^\dagger_{\boldsymbol{k}\lambda} b_{\boldsymbol{k}\lambda}\rangle(t) \\ &= \frac{2}{\hbar\epsilon_0}\sum_i^N \mathrm{Im}\Bigg[\sum_\lambda \int d\boldsymbol{k} \frac{\omega_{\boldsymbol{k}}\boldsymbol{d}_i\cdot\boldsymbol{f}^*_{\boldsymbol{k}\lambda}(\boldsymbol{r}_i)\boldsymbol{f}_{\boldsymbol{k}\lambda}(\boldsymbol{r}_i)\cdot\boldsymbol{d}_i}{16\pi^3(\omega_{\boldsymbol{k}}-\omega)}\langle\sigma^i_{10}\sigma^i_{01}\rangle \\ &\quad + \sum_{j\neq i}^N\sum_\lambda \int d\boldsymbol{k} \frac{\omega_{\boldsymbol{k}}\boldsymbol{d}_j\cdot\boldsymbol{f}^*_{\boldsymbol{k}\lambda}(\boldsymbol{r}_j)\boldsymbol{f}_{\boldsymbol{k}\lambda}(\boldsymbol{r}_i)\cdot\boldsymbol{d}_i}{16\pi^3(\omega_{\boldsymbol{k}}-\omega)}\langle\sigma^i_{10}\sigma^j_{01}\rangle\Bigg] \\ &= \frac{2}{\hbar\epsilon_0}\sum_i^N \mathrm{Im}\big[\boldsymbol{d}_i\cdot\boldsymbol{G}(\boldsymbol{r}_i,\boldsymbol{r}_i,\omega_i)\cdot\boldsymbol{d}_i\langle\sigma^i_{10}\sigma^i_{01}\rangle\big] \\ &\quad + \frac{2}{\hbar\epsilon_0}\sum_{i\neq j}^N\sum_{j\neq i}^N \mathrm{Im}\big[\boldsymbol{d}_j\cdot\boldsymbol{G}(\boldsymbol{r}_j,\boldsymbol{r}_i,\omega_i)\cdot\boldsymbol{d}_i\langle\sigma^i_{10}\sigma^j_{01}\rangle\big]. \end{aligned} \tag{9}$$

Next, we explain how to renormalize the information on the environmental structure in the Green's function. To convolve the effect of the environmental (metallic) structure, we solve

$$\boldsymbol{G}(\boldsymbol{r},\boldsymbol{r}',\omega) = \boldsymbol{G}_0(\boldsymbol{r},\boldsymbol{r}',\omega) + \int d\boldsymbol{r}''\boldsymbol{G}_0(\boldsymbol{r},\boldsymbol{r}'',\omega)\chi(\boldsymbol{r}'',\omega)\boldsymbol{G}(\boldsymbol{r}'',\boldsymbol{r}',\omega) \tag{10}$$

numerically [36], where $\boldsymbol{G}_0$ is the dyadic Green's function in a vacuum and χ is the susceptibility of the material that forms the environmental structure. By using the discrete dipole approximation (DDA) [37] to solve this equation, we can obtain the Green's function for arbitrary geometric structures of environmental materials. In the calculation of the DDA, we recast Eq. (10) as a set of simultaneous equations of Green's functions for discretized cells as

$$\begin{aligned} \boldsymbol{G}^0_{ij} &= \boldsymbol{G}_{ij} - \sum_{j'} V\boldsymbol{G}^0_{ij'}\chi_{j'}\boldsymbol{G}_{j'j} \\ &= \sum_{j'}\big(\delta_{ij'}\boldsymbol{I} - V\boldsymbol{G}^0_{ij'}\chi_{j'}\big)\boldsymbol{G}_{j'j} \\ &= \sum_{j'}\boldsymbol{A}_{ij'}\boldsymbol{G}_{j'j}, \end{aligned} \tag{11}$$

where i and j are the indices of the discretized cells; $\boldsymbol{G}^0_{ij}$ and $\boldsymbol{G}_{ij}$ are discretized versions of $\boldsymbol{G}_0(\boldsymbol{r},\boldsymbol{r}')$ and $\boldsymbol{G}(\boldsymbol{r},\boldsymbol{r}')$, respectively; and $\boldsymbol{I}$ and V are the dyad and the volume of a single cell, respectively.

Here, we describe our calculation model. In this study, we constructed a reference model to examine the fluorescence of parallel and antiparallel combinations of chiral structures. Figure 1 shows the calculation model. This system featured a chiral emitter assembly that was combined with a spirally stacked metallic structure, as shown in the diagram in Fig. 1(a). The size of one piece of metal was 35 nm ×35 nm ×5 nm, and the values of z shown in Fig. 1(b) indicate the positions occupied by each piece of metal on the z axis. The size of the square channel along the z axis in the center was 25 nm × 25 nm. There was also a spiral emitter assembly, which consisted of 18 emitters, located at the center. Although larger structures may exhibit more significant effects, we limited ourselves to this size because of the computational load. Even if a pure chirality effect was dominant in the actual experiments, it would not be easy to identify if there were other effects arising from various kinds of fluctuations. Hence, the theoretical examination of the effect plays a significant role in excluding such effects through the utilization of the exact structure. To this end, we carefully designed the model system so that the distances between respective emitters and the pieces of metal nearest to them were equal for both the parallel and antiparallel combinations. We also ensured the same was true for the sum of these distances. Therefore, the field enhancement effect was exactly the same for both combinations of chirality (see Appendix A for details). The effects of the possible structural fluctuations that would appear in the actual experiments are examined in Appendix C. In addition, we assumed the polarizations of the emitters in each layer were isotropic in the xy plane. Specifically, we placed two emitters with uniaxial polarizations in the same location so that their polarizations were orthogonal [Fig. 1(b)]. The proposed structure is a layer-by-layer structure, and hence, the state-of-the-art fabrication and manipulation technologies would be able to produce structures similar to it [38]. Further, this simple planar-type model helped extract pure chirality-selective effects and subsequently boost superfluorescence because it is easy to set up parallel and antiparallel structures with the same field enhancement effect. Material parameters are described in Appendix B.

In our previous study, we developed the theoretical framework to study the synchronization effects of arbitrarily configured emitters in arbitrary dielectric environments [34].

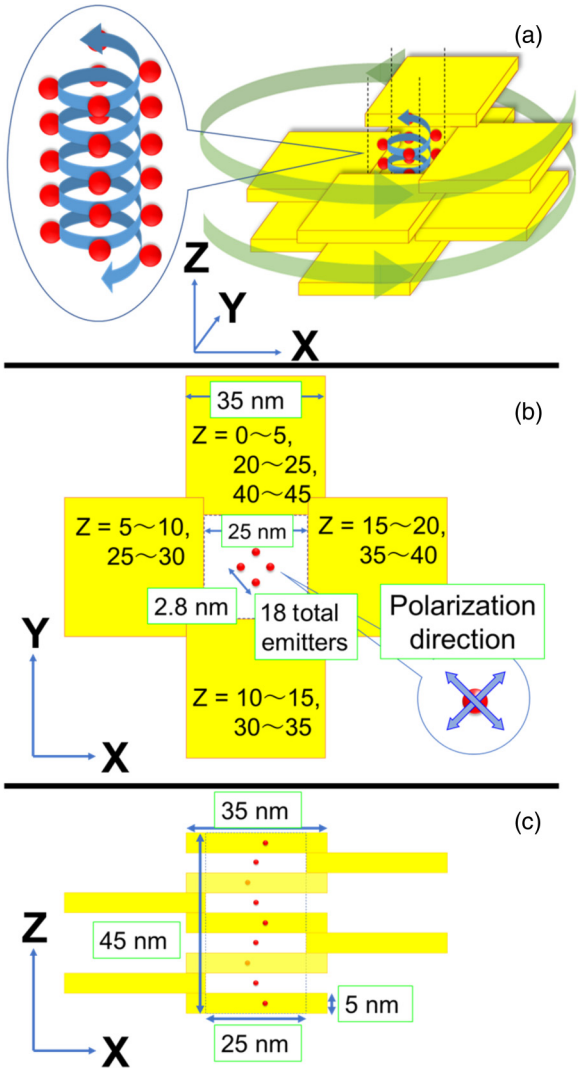

FIG. 1. (a) Diagram of the calculation model. The metallic structures were stacked to allow left-handed and right-handed structures to be drawn around the z axis. The light emitters were also arranged in the same way. (b) Top view and (c) side view of the calculation model. The value of z in the figure indicates the position of each piece of metal for the left-handed structures in the direction of the z axis. The polarization of the emitters in each layer was isotropic in the xy plane.

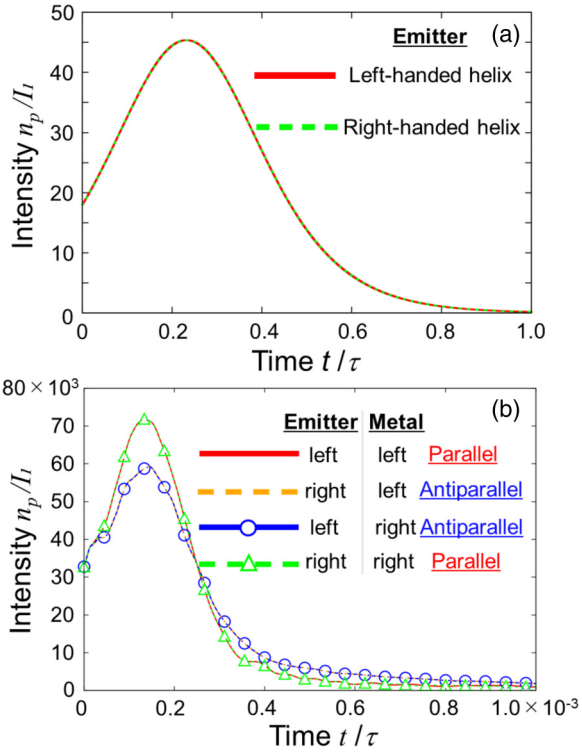

FIG. 2. The time profile of the intensity of the superfluorescence for the following two conditions: (a) the chiral emitter assembly in a vacuum and (b) the chiral emitter assembly surrounded by the chiral metallic structures. I_1 is the initial value of the intensity of one emitter in a vacuum. We normalized the emission intensity n_p [in Eq. (9)] using I_1. We also normalized the time using τ (0.27 ns), which is the radiative lifetime of the emitter in a vacuum.

This revealed a superfluorescence arising from the enhanced correlation that occurred via the confined radiation modes. In the model used in the present study, a different type of enhancement was expected to originate from the enhanced chiral field via plasmonic resonance. For a clear demonstration of chirality-selective effects, we chose the parameters for quantum dots with larger dipole moments among those reported to exhibit superfluorescence with less than ten particles within one wavelength [39]. Considering this point and the plasmonic resonance energy of the model used in this study, we assumed the dipole moment to be 47.5 D and the resonant energy to be 1.0 eV. Regarding decoherence and nonradiative decay channels, we do not explicitly include them in this model. It is known that if $\sqrt{\tau_R \tau_D} < T_2$, superfluorescence (SF) occurs [40], where τ_R, τ_D, and T_2 correspond to the cooperatively radiative decay time of populations in excited states of emitters, the onset time for cooperative emission, and the dephasing time determined by the pure dephasing and nonradiative population decay, respectively. In the present study, we consider the case where $\sqrt{\tau_R \tau_D}$ is significantly shorter than T_2 because of the plasmonic boosting of cooperation of emission. Thus, the decoherence and the nonradiative decay do not play an essential role though they might reduce the intensity of SF to some extent.

III. RESULTS

In the following calculations, we examined the fluorescence dynamics just after the strong excitation of the system. Thus, we adopted the initial conditions $\langle \sigma_{10}^i \sigma_{01}^i \rangle = 1$ and $\langle \sigma_{10}^i \sigma_{01}^j \rangle = 0$ for Eqs. (7) and (8), respectively. Namely, we assumed that all the emitters are in the excited state and that there is no correlation between the emitters at the initial stage. We normalized the time using the radiative lifetime of the emitter τ in a vacuum, which is 0.27 ns for the present parameter of the dipole moment. Figure 2(a) shows the time profile of the emission intensity of the chiral emitters in the absence of the metallic structures. The results show the typical time profiles of the superfluorescence; in this case, the

left-handed and right-handed structures have the same time profiles. Figure 2(b) shows the time profiles for the chiral emitters that were surrounded by the chiral metallic structures. The emission intensity was increased by several orders of magnitude compared to that in the absence of the metallic structures.

This large enhancement in the superfluorescence was due to the enhanced field that was generated via plasmonic resonance, which caused the correlations between the emitters to be strengthened significantly. The identification of the field enhancement effect for both combinations can be verified by the fact that the initial intensities of the fluorescence for both combinations were exactly the same. In contrast, the peak values of the intensity for the parallel and antiparallel systems were different. In the calculation model, this difference was about 20%, which represents a value approximately 300 times larger than the peak value of the superfluorescence in the absence of the metallic structures. As mentioned above, the field enhancement effect equally affected the emitters in the parallel and antiparallel systems. Therefore, we conclude that the growth of the correlation between the emitters plays a significant role in chirality-selective superfluorescence. In particular, because of the mutual interplay between the two kinds of chiralities (that of the emitters and that of the metallic structure), the parallel system exhibits stronger correlation and more superfluorescence than the antiparallel system. Then, the main problem that is to be elucidated is how the parallel combination greatly enhances the superfluorescence. (Here, we do not compare these results with those of an achiral emitter assembly in the chiral metallic structures because it is difficult to set up the condition with the same field enhancement effect as that of the chiral case.)

IV. DISCUSSIONS

A. Role of correlations

To address the aforementioned issue, we examined the role of correlations in chirality-selective superfluorescence. First, we examined the case in which we reduced the dipole moment to 27.4 D (we increased the radiative lifetime of the emitter by a factor of 3). Namely, this case assumes a weak correlation between emitters. Figure 3(a) shows the time profile of the superfluorescence under this condition. Although the intensity and the decay time were boosted by the Purcell effect [41], namely, the spontaneous emission rate is enhanced by the enhanced field near the metallic structures, the characteristics of superfluorescence were imperceptible in this case. Importantly, almost no chirality-selective behavior was detected. This indicates that the chiral selectivity was triggered only through the correlation between the emitters. Furthermore, we examined the system in which we neglected the correlation terms in the calculation. In this case, the time profiles for both combinations of chirality became entirely those of boosted spontaneous emission caused by the Purcell effect, and no difference appeared between them [Fig. 3(b)]. These results suggest that the difference in superfluorescence caused by chirality arose from the different quantum correlations that appeared according to the combination of the chiralities of the emitters and metallic structures. Thus, in the present model, the field enhancement effect of the localized surface plasmons

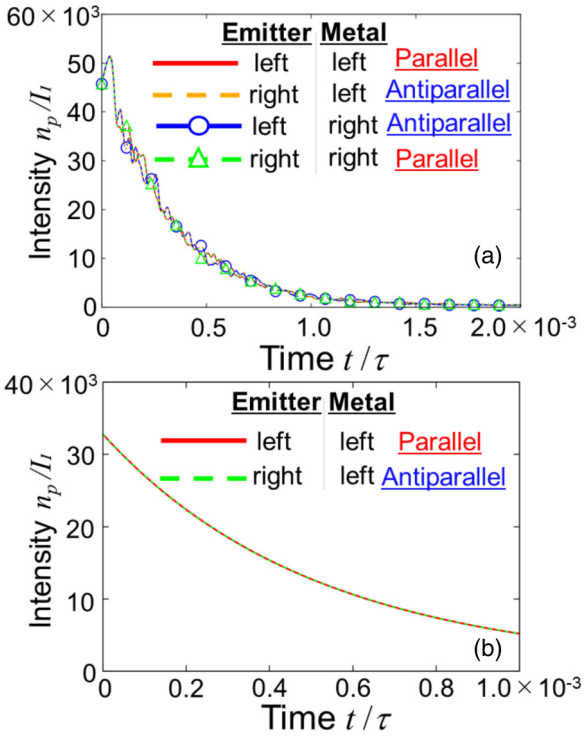

FIG. 3. (a) The time profile of the intensity of the superfluorescence when there is weak correlation between the emitters. (b) Time profile of the intensity of the superfluorescence when there is no correlation between the emitters.

alone did not cause the difference in superfluorescence between the different combinations of chiralities.

We analyzed the chirality-selective behavior of the correlations through the following procedure. We divided the whole system into nine layers, as shown in the legend of Fig. 4(a). Let us represent the correlation $\langle \sigma_{10}^{i} \sigma_{01}^{j} \rangle$ between the emitters in the parallel (antiparallel) combination as $C_{i,j}^{\mathrm{par(ant)}}$. In addition, consider $\tilde{C}_i^{\mathrm{par(ant)}} = \sum_{j(\neq i)} |C_{i,j}^{\mathrm{par(ant)}}|$. The time profile of $\tilde{C}_i^{\mathrm{par}}$-$\tilde{C}_i^{\mathrm{ant}}$ is plotted in Fig. 4(a), which shows that at approximately $t/\tau = 0.0002$, where the emission intensity peaks [Fig. 2(b)], the correlations for the parallel case were more strongly enhanced than those for the antiparallel case. In particular, $\tilde{C}_i$ near both sides of the stacked structures exhibited a large difference between the parallel and antiparallel cases. The maximum value of the correlation also demonstrated a clear difference [Fig. 4(b)]. In the parallel case, the maximum value of correlation was lower in the first and ninth layers than in the other layers. In the antiparallel case, a similar tendency was observed in additional layers (i.e., the first, second, eighth, and ninth layers). Rather than having a uniform correlation throughout the illuminant, the correlation between the emitters exhibited local differences within the whole structure. Thus, the key to understanding the chirality-selective enhancement of superfluorescence is the local behavior of the correlation.

B. Local behavior of correlations

For a given layer, each emitter's excited-state occupation as a function of time behaved differently for the parallel and

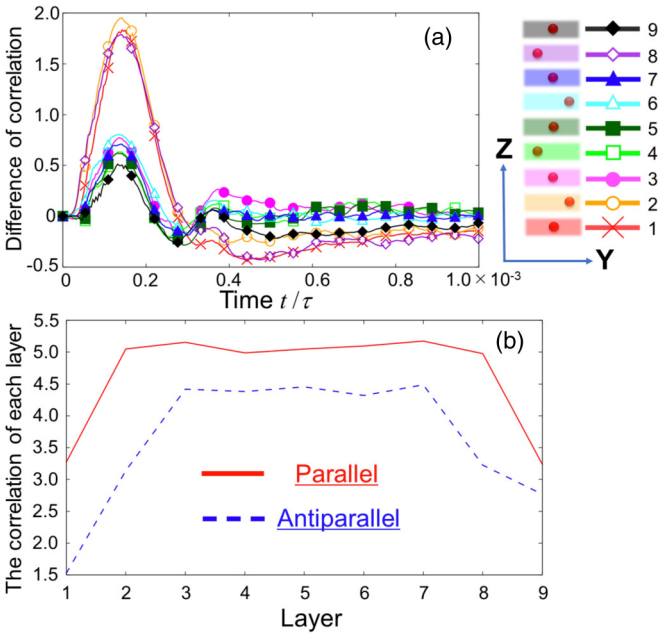

FIG. 4. (a) Time variation of the absolute value of the correlation $\tilde{C}_i^{\rm par}$-$\tilde{C}_i^{\rm ant}$ for each layer i. The shading of the lines and the types of symbols in the graph correspond to the positions of the emitters shown in the legend. (b) Maximum value in the time variation of the correlations $\tilde{C}_i^{\rm par}$ and $\tilde{C}_i^{\rm ant}$ for each layer i. For all layers, the parallel system has a stronger correlation between the emitters.

antiparallel cases. Figures 5(a) and 5(b) show the time variation of the excited-state occupation for each of the 18 emitters in the parallel and antiparallel cases. As shown in Fig. 5(a), 16 emitters decayed quickly and the 2 emitters at the edge layers decayed much more slowly than the other 16. In contrast,

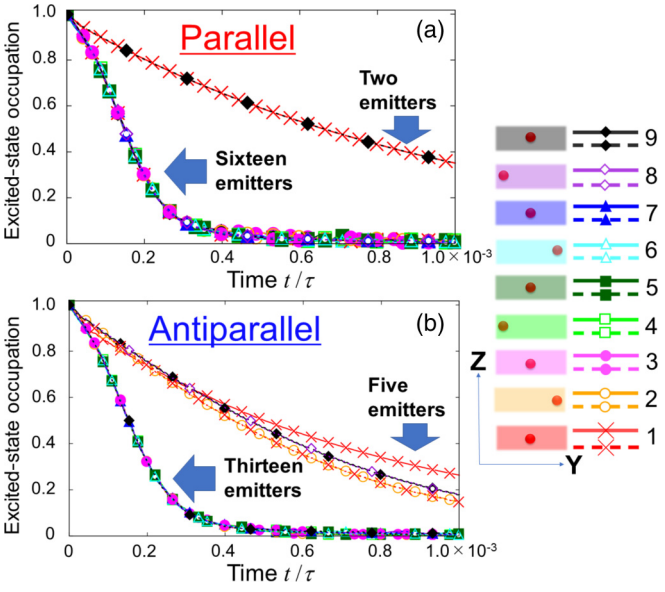

FIG. 5. Time variation of the excited-state occupation of each emitter for the (a) parallel and (b) antiparallel combinations of the chiral structures. The numbers in the legend indicate the emitter layer on which the detector was placed. Solid and dotted lines of the same color indicate emitters in the same layer.

Fig. 5(b) shows that the 5 emitters at the two edge layers decayed more slowly than the other 13. This result indicates that the correlation between the emitters was easier to form for the parallel case and that a higher number of emitters contributed to the superfluorescence. This local imbalance in creating correlations between the parallel and antiparallel combinations was significant for the chirality-selective superfluorescence.

Next, we examine how the local imbalance in creating correlations occurred by examining the polarization distribution in the local field around the emitters. The calculation model is shown in Figs. 6(a) and 6(b). The whole structure was divided into nine layers in the z direction, and we placed a detector in each layer and calculated the polarization distribution of each layer (the position of the detector in the xy plane was the center of the system). The detector was modeled by an emitter with a specific polarization direction. Its dipole moment was set to be small so that it did not affect the fluorescent behavior of the other emitters. (We reduced the dipole moment to 47.5×10^{-3} D.) After setting the detector's initial excitation occupation to 0 [$\langle\sigma_{10}^D\sigma_{01}^D\rangle=0$ for Eq. (7)], we monitored the occupation in the time domain. By changing the direction of the detector polarization, we obtained the polarization distribution of the local field in each layer. Figures 6(c) and 6(d) show the results. For the parallel case shown in Fig. 6(c), the first and ninth layers, which were located at the edges of the structure, had a strong polarization component in a direction different from that of those in layers 2–8. In contrast, for the antiparallel case shown in Fig. 6(d), the polarization components in layers 1, 2, 8, and 9 were significantly different from those in other layers. There was no significant difference in the polarization distributions between layers 2–8 (in the parallel case) and layers 3–7 (in the antiparallel case). The y component was slightly stronger due to the fact that the geometrical relation between the chiral emitter assembly and the chiral metallic structures was not xy symmetric even though the effect of the localized field was completely identical for all the emitters. As shown in Fig. 1(b), the emitters in each layer were isotropic in the xy plane in terms of polarization. However, for the polarization distributions for the respective (independent) two-layer structures [Figs. 6(e), 6(f), and 6(g)], the polarization was as strongly biased as those at the edges of the structure. Thus, we know that the polarization distributions were aligned by a cooperative effect due to the correlation between the layers, particularly the inner layers, and this generated strong superfluorescence. However, this alignment was not sufficient at the edge layers. Furthermore, this insufficiency was larger for the antiparallel case because it had a lower correlation compared to that of the parallel case. Thus, the local chirality-induced differences seen in the correlation caused large differences in the emission intensities, which can be seen in Fig. 2(b). We expect that this elucidation of the mechanism will lead to the guiding principle for exploiting more chirality-selective superfluorescence phenomena and their applications.

V. SUMMARY AND CONCLUSION

In summary, we have demonstrated a chirality-selective enhancement of superfluorescence by using a model of spirally

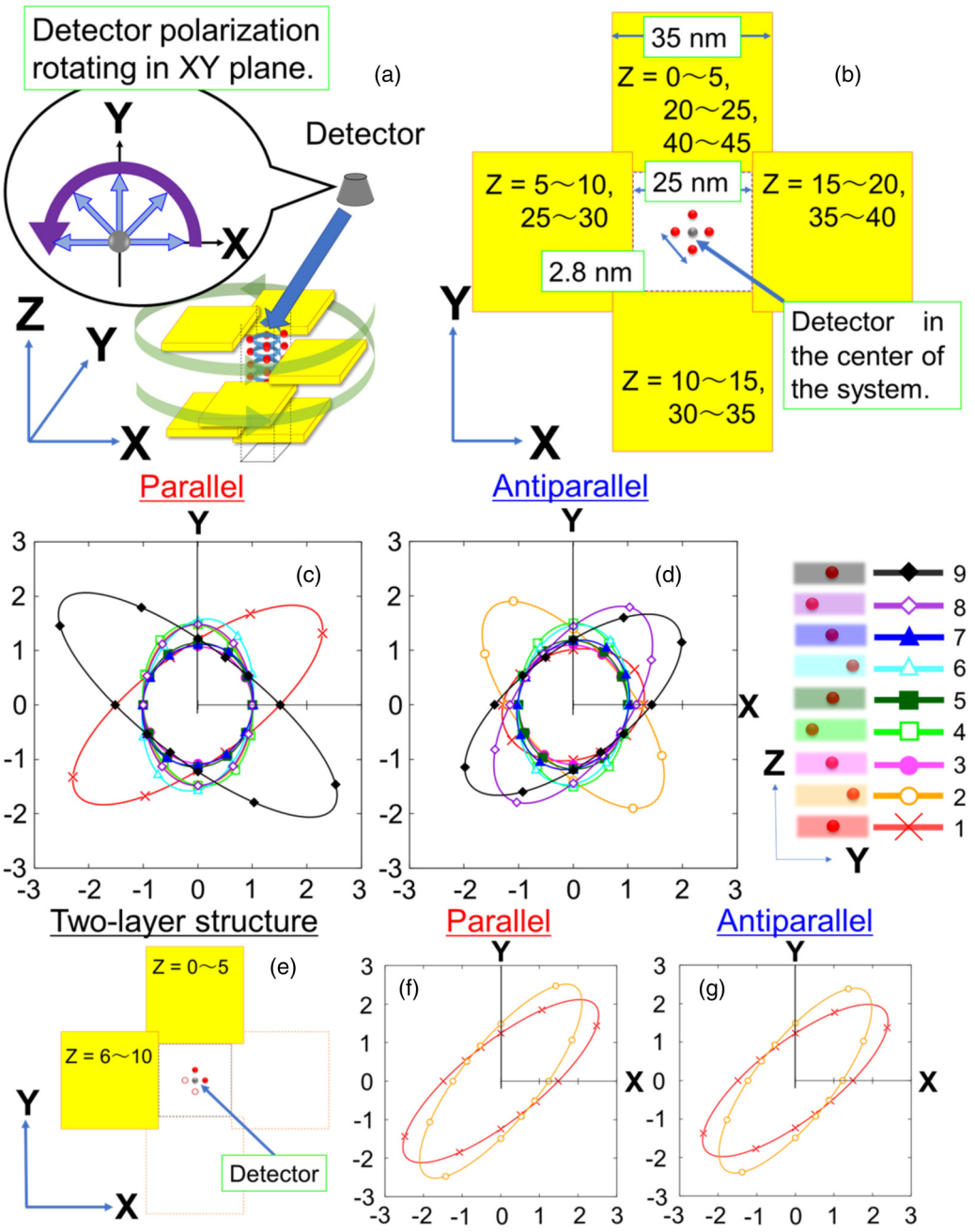

FIG. 6. (a) Calculation model for the polarization distribution in the local field of the emitters. As indicated by the callouts in the figure, the direction of the polarized axis (light-colored arrows) of this detector rotates in the *xy* plane. (b) Top view of the calculation model. We placed the detector at the center of the calculation model in the *xy* plane. For graphs (c), (d), (f), and (g), the polarization distribution in the fluorescent field (estimated from the excited-state occupation in the time domain for each polarization direction of the detector) is plotted. The distance from the origin to each point on the circle indicates the estimated intensity of the field when the detector's polarization is parallel to the line from the origin to this point. The colors and symbols of the lines in the graphs represent the layers on which the detector was placed. The numbers in the legend indicate the corresponding layers. For each layer, the magnitude of the polarization distribution in the *xy* plane was normalized according to the length of the short axis. Polarization distribution in the local field of the emitters for the case of (c) parallel and (d) antiparallel combinations of chiral structures. (e) Top view of the calculation model with only two layers (the placement of the pieces of metal and the emitters indicates the parallel configuration). Polarization distribution in the local field of the emitters for a two-layer structure for the (f) parallel and (g) antiparallel cases.

arranged emitters and stacked metallic structures. To extract a pure chirality effect, we carefully designed the model so that the effect of the plasmonic resonance-induced local field enhancement on the emitter assembly was strictly the same for the parallel and antiparallel chiral configurations of the emitter assembly and surrounding metallic structures. The superfluorescence of the chiral emitter assembly was significantly enhanced by the surrounding metallic structures because of the localized surface plasmon resonance. Furthermore, for the parallel configuration, the enhancement was greater than

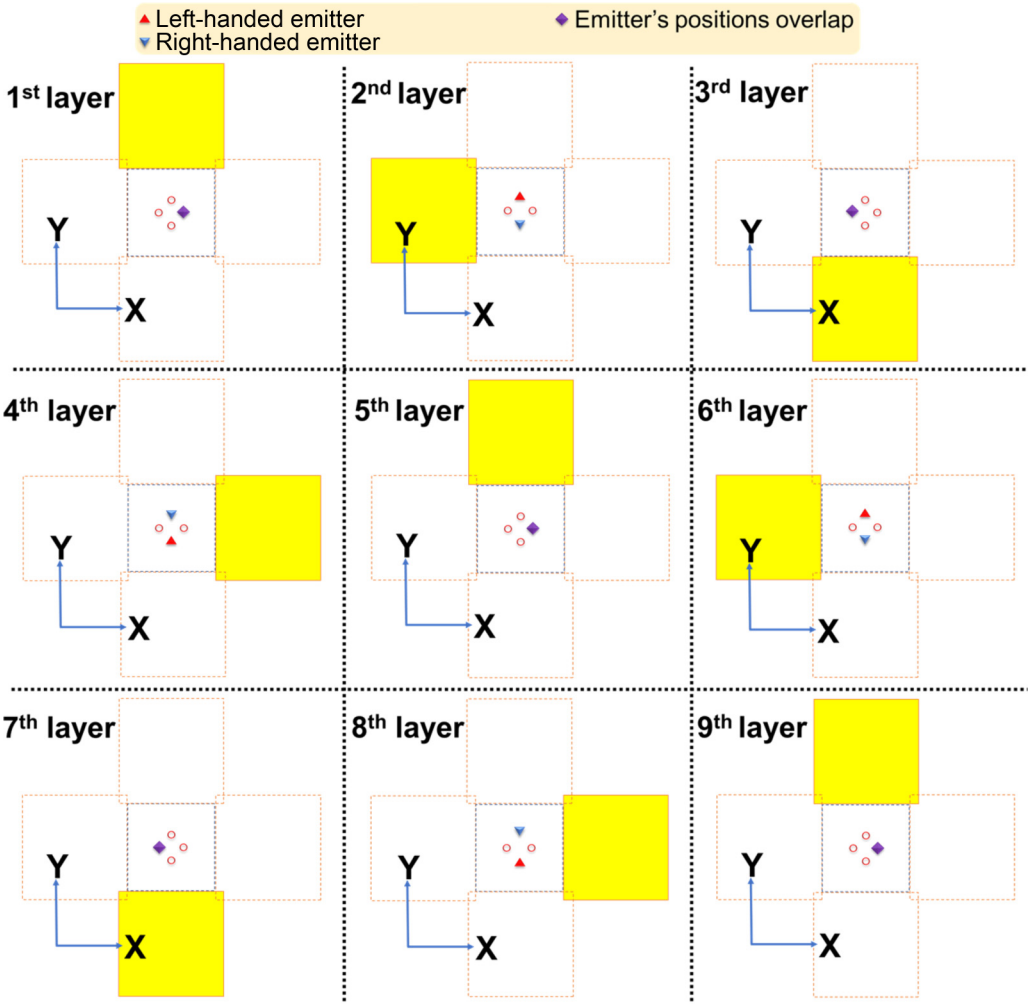

FIG. 7. Arrangement of the emitters and metal pieces for each layer. These figures show the arrangement of the metal pieces in the left-handed chiral metal structure.

that for the antiparallel configuration. This chirality-selective enhancement of the superfluorescence occurred because the quantum correlations between the emitters were stronger for the parallel configuration. In this cooperative process, the polarization distributions of the different layers were aligned.

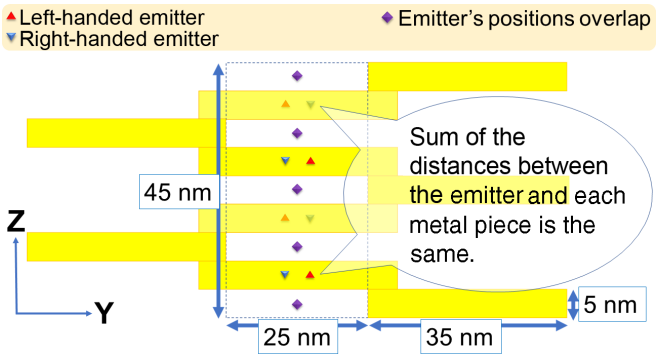

FIG. 8. The side view of the calculation model. Compare each emitter of the left- and right-handed helix that the callouts indicate; the sum of the distances between the emitter and each metal piece is the same.

However, this alignment was weaker in the antiparallel case than it was in the parallel case.

Although in this study we employed a specific model, we discovered the general mechanism behind chirality-selective many-body cooperative effects; that is, the chiral interplay between the matter system and the immediate environment creates chirality-selective superfluorescence. This finding will contribute to elucidation of the mechanism of chiral interaction between matter systems and field as environment from a fundamental viewpoint, as well as to the development of various applications such as highly sensitive chiral sensing techniques and chiral light source [42] based on the cooperative emission. Despite the fact that the results revealed the general mechanism behind chirality-selective cooperative effects, the model presented in this study is limited to a specific set of material parameters. In the level structure of emitters, this study deals with independent two-level systems, but when dealing with multilevel systems, we can expect a further impact on superfluorescence [26,43]. Hence, to explore more efficient and robust effects, further studies on additional types of system designs with different shapes, sizes, and types of emitters are required. We expect that the findings of this study will trigger future theoretical and experimental studies.

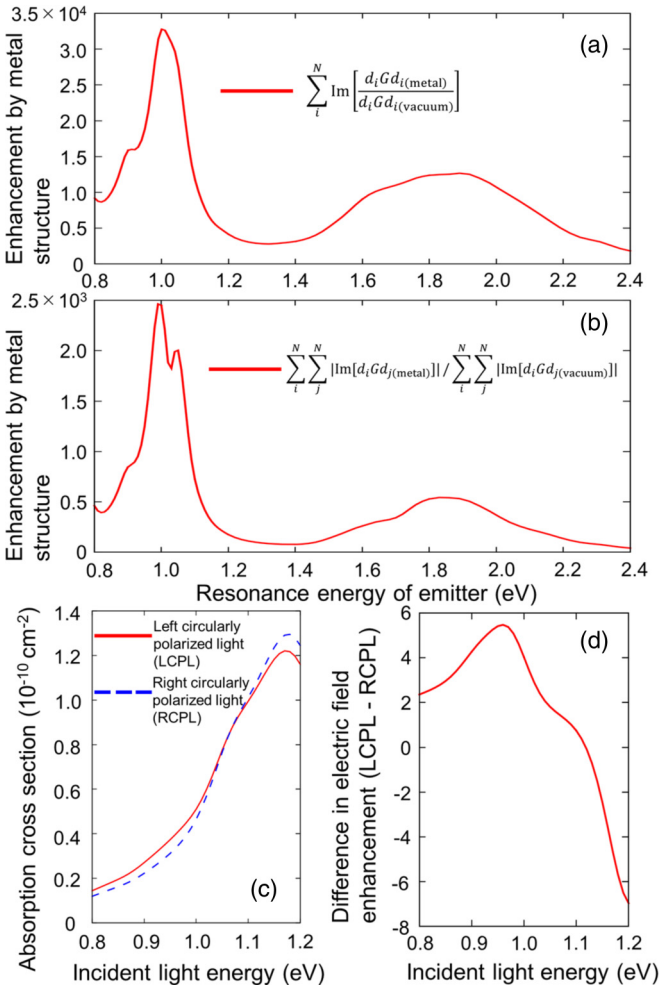

FIG. 9. (a) Spectrum of enhancement in $\boldsymbol{d}_i \cdot \boldsymbol{G} \cdot \boldsymbol{d}_i$ in Eq. (9). (b) Spectrum of enhancement in $\boldsymbol{d}_i \cdot \boldsymbol{G} \cdot \boldsymbol{d}_j$ in Eq. (9). (c) Spectra of the absorption cross section of the spirally arranged metallic structures. We calculate the absorption cross section across the entire metal structure. (d) Spectrum of the differences in the enhancement of the electric field ($|\boldsymbol{E}|^2/|\boldsymbol{E}_0|^2$). The electric field intensity at all the emitters' positions are summed. $|\boldsymbol{E}|^2$ is in the presence of the metallic structure and $|\boldsymbol{E}_0|^2$ is in a vacuum. (c, d) The left-handed metal structure (not including the spirally configured emitters) was irradiated with left- or right-circularly polarized light. The incident light propagated in the direction of the positive z axis.

ACKNOWLEDGMENTS

This work was supported in part by JSPS KAKENHI Grant No. JP16H06504 for Scientific Research on Innovative Areas "Nano-Material Optical-Manipulation" and by JSPS KAKENHI (Grants No. JP21H05019, No. JP22J14274, and No. JP22H05132).

APPENDIX A: DETAILS OF THE MODEL SYSTEM

In this study, we consider a sort of "ideal model" in which the distance between each emitter and its nearest metal piece is equal for parallel and antiparallel combinations. Then, neglecting the correlations between the emitters, the entire metal structure should act on the fluorescence for both the combinations equally. One can confirm the equivalent effect of the plasmon-induced field enhancement for the different combinations of chiral structures by exactly the same rising behaviors of the emission time profile in Fig. 2(b) in the main text. With this model, we extract the effect of chirality coupling on the formation of the correlations between the emitters. The specific configuration is described below.

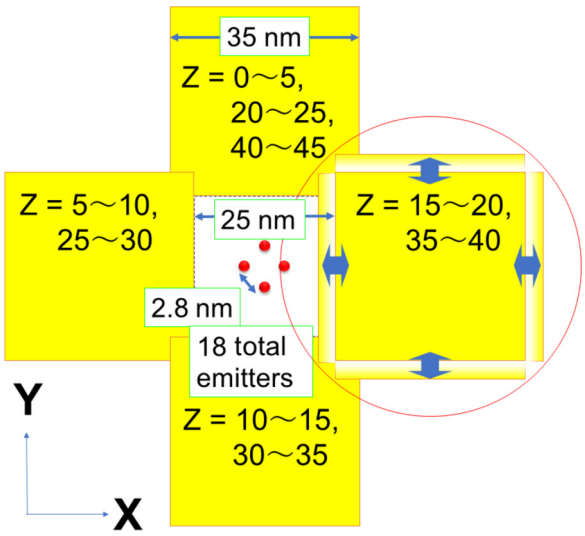

FIG. 10. Schematic of sample fluctuations of metallic structures. We shift the position of each metal piece by 1 nm according to the Gaussian distribution in the xy plane.

Figure 7 shows the arrangement of the emitters and a metal piece in each layer for the left-handed chiral metal structure. The arrangement of each layer has four patterns. The position of the nth emitter (in the nth layer), with the center of the metallic structure as the origin, can be expressed as follows: $\boldsymbol{r}_n = [2\sin(\frac{\pi n}{2}), \mp 2\cos(\frac{\pi n}{2}), 5n - 2]$ (nm). Here $\mp$ represents the left-handed and right-handed rotation of the helix direction of the emitters. In the odd layers, the positions of the emitters are the same for the left- and right-handed helix. In the even layers, although the positions of the emitters are different, the distances between the respective emitters and the nearest metal piece are the same. We construct the entire structure with nine layers as shown in Fig. 8 so that the sum of the distances between respective emitters and metal pieces is equal for the parallel and antiparallel combinations. For example, the sum of the distances between the emitter in the second layer and the metal pieces is different for the left-handed helix and the right-handed helix. However, comparing the emitter located at the second layer in the left-handed helix and the emitter located at the eighth layer in the right-handed helix, the respective sums of the distances between the respective emitters and metal pieces are the same. For other layers, there are layers where the sum of the distance between the emitter and the metal pieces is the same. Considering all the emitters and metal pieces, the sum of their distances is designed to match in either combination. The identification of the field enhancement effect for both combinations can be verified by the fact that the initial intensities of the fluorescence for both combinations were exactly the same as seen in Fig. 2(b) in the main text.

APPENDIX B: PARAMETERS OF EMITTERS AND METAL STRUCTURES

Regarding the parameters of the emitters, we assume quantum dots with a resonance energy of 1.0 eV and a dipole moment of 47.5 D. We assume that the metal is Au, and the dielectric constant is given by the Drude model, which is expressed as

$$\chi(\omega) = \epsilon_{\mathrm{Au}} - 1.0 - \frac{\omega_{\mathrm{Au}}^2}{\omega^2 + i\omega\left(\gamma_{\mathrm{bulk}} + \frac{\nu}{L_{\mathrm{eff}}}\right)}, \tag{B1}$$

where ϵ_{Au} is the background dielectric constant of Au, $\hbar\omega_{\mathrm{Au}}$ is the bulk plasma frequency, $\hbar\gamma_{\mathrm{bulk}}$ is the electron-relaxation constant, ν is the electron velocity at the Fermi level, and L_{eff} is the effective mean free path of the electrons. We use the following parameter values: $\epsilon_{\mathrm{Au}} = 12.0$, $\hbar\omega_{\mathrm{Au}} = 8.958$ eV, $\hbar\gamma_{\mathrm{bulk}} = 72.3$ meV, $\nu = 0.9215$ nm eV, and $L_{\mathrm{eff}} = 20$ nm [44]. In this demonstration, we choose the resonance energy of emitters so that it is covered by the resonance peak of the spectra of $\boldsymbol{d}\cdot\boldsymbol{G}\cdot\boldsymbol{d}$ values [Eq. (9)] shown in Fig. 9(a) for the metallic structure depicted in Fig. 1 in the main text. Figures 9(a) and 9(b) indicate that a strong enhancement occurs for $\boldsymbol{d}\cdot\boldsymbol{G}\cdot\boldsymbol{d}$ values around 1.0 eV. Figure 9(c) shows the spectra of the absorption cross sections of the spirally arranged metallic structures, and Fig. 9(d) shows the difference between the enhancement in the electric field at the position of the spirally arranged emitters when the left-handed metal structure is irradiated with left- or right-circularly polarized light. The incident light propagates in the direction of the positive z axis. In both figures, the difference appears when the incident light has an energy of approximately 1.0 eV as well as the intensity of superfluorescence.

APPENDIX C: INFLUENCE OF SPATIAL FLUCTUATIONS OF CHIRAL METALLIC STRUCTURES ON CHIRALITY-SELECTIVE SUPERFLUORESCENCE

Here, we examine how the sample fluctuations affect the appearance of the chirality-selective superfluorescence. Although there are some types of sample fluctuations, we consider the positional fluctuations of metal blocks in the xy plane that would influence the effect arising from plasmonic enhancement most seriously. As shown in Fig. 10, we shift the position of some randomly chosen metal pieces among nine [Fig. 7(a)] according to the Gaussian distribution in the xy plane. Since a side of the cell cube of DDA calculation is 1 nm, the positional shift of each metal piece toward one direction is by 1 nm. Considering such fluctuations of the position of the metal pieces, we compare the emission intensity in the parallel and antiparallel cases. We calculated 50 trials with a variance value in a Gaussian distribution of $\sigma^2 = 0.25$. For this variance value, the average of the total fluctuations in the position of the nine metal pieces is about 3.8 nm. In this case, the average difference in maximum value of emission intensity between the parallel and antiparallel cases is about 5.2%. This average difference in emission intensity is about 50 times larger than the peak value of the superfluorescence in itself in the absence of the metallic structures [in Fig. 2(a) in the main text]. Thus, the difference in chirality-selective enhancement in emission intensity is significant even for this case. For 50 trials with a variance value in a Gaussian distribution of $\sigma^2 = 0.5$ (in this case, the average of the total fluctuations in the position of the nine metal pieces is about 8.2 nm), the average difference in maximum value of emission intensity between the parallel and antiparallel cases is about 1.3%. The origin of this decrease of emission difference is more rapid reduction of the correlation among emitters for the parallel case than for the antiparallel case due to fluctuation. This difference is still larger than the peak value in the absence of the metallic structures and an ensemble of this composite structure would show a significant chiral selectivity. However, we understand from this result that a fluctuation smaller than $\sigma^2 = 0.5$ is favorable for the clear observation of chirality-selective superfluorescence. Note that the reason for this seemingly severe condition is due to the smallness of the calculation model. The relative accuracy of the fabrication of a larger system is much higher. Thus, this required condition is not so hard as in this demonstration in reality.

[1] L. D. Barron, Nature (London) **405**, 895 (2000).
[2] L. D. Barron, Chirality **24**, 879 (2012).
[3] L. D. Barron, M. P. Bogaard, and A. D. Buckingham, J. Am. Chem. Soc. **95**, 603 (1973).
[4] S. F. Mason, Nature (London) **311**, 19 (1984).
[5] G. L. J. A. Rikken and E. Raupach, Nature (London) **405**, 932 (2000).
[6] E. Hendry, T. Carpy, J. Johnston, M. Popland, R. V. Mikhaylovskiy, A. J. Lapthorn, S. M. Kelly, L. D. Barron, N. Gadegaard, and M. Kadodwala, Nat. Nanotechnol. **5**, 783 (2010).
[7] A. Kuzyk, R. Schreiber, Z. Fan, G. Pardatscher, E.-M. Roller, A. Högele, F. C. Simmel, A. O. Govorov, and T. Liedl, Nature (London) **483**, 311 (2012).
[8] C. Song, M. G. Blaber, G. Zhao, P. Zhang, H. C. Fry, G. C. Schatz, and N. L. Rosi, Nano Lett. **13**, 3256 (2013).
[9] Y. Liu, W. Zhao, Y. Ji, R.-Y. Wang, X. Wu, and X. Zhang, Europhys. Lett. **110**, 17008 (2015).
[10] L. M. Kneer, E.-M. Roller, L. V. Besteiro, R. Schreiber, A. O. Govorov, and T. Liedl, ACS Nano **12**, 9110 (2018).
[11] Q. Zhang, T. Hernandez, K. W. Smith, S. A. H. Jebeli, A. X. Dai, L. Warning, R. Baiyasi, L. A. McCarthy, H. Guo, D. H. Chen, J. A. Dionne, C. F. Landes, and S. Link, Science **365**, 1475 (2019).
[12] J. Mun, M. Kim, Y. Yang, T. Badloe, J. Ni, Y. Chen, C.-W. Qiu, and J. Rho, Light Sci. Appl. **9**, 139 (2020).
[13] K. Martens, F. Binkowski, L. Nguyen, L. Hu, A. O. Govorov, S. Burger, and T. Liedl, Nat. Commun. **12**, 2025 (2021).
[14] K. Toyoda, K. Miyamoto, N. Aoki, R. Morita, and T. Omatsu, Nano Lett. **12**, 3645 (2012).
[15] J. Ni, C. Wang, C. Zhang, Y. Hu, L. Yang, Z. Lao, B. Xu, J. Li, D. Wu, and J. Chu, Light Sci. Appl. **6**, e17011 (2017).

[16] K. Masuda, R. Shinozaki, Y. Kinezuka, J. Lee, S. Ohno, S. Hashiyada, H. Okamoto, D. Sakai, K. Harada, K. Miyamoto, and T. Omatsu, Opt. Express **26**, 22197 (2018).
[17] S. G. Ray, S. S. Daube, G. Leitus, Z. Vager, and R. Naaman, Phys. Rev. Lett. **96**, 036101 (2006).
[18] B. Göhler, V. Hamelbeck, T. Markus, M. Kettner, G. Hanne, Z. Vager, R. Naaman, and H. Zacharias, Science **331**, 894 (2011).
[19] R. Naaman and D. H. Waldeck, J. Phys. Chem. Lett. **3**, 2178 (2012).
[20] U. Huizi-Rayo, J. Gutierrez, J. M. Seco, V. Mujica, I. Diez-Perez, J. M. Ugalde, A. Tercjak, J. Cepeda, and E. San Sebastian, Nano Lett. **20**, 8476 (2020).
[21] A.-C. Cheng, H. Niinomi, T. Omatsu, S. Ishida, K. Sasaki, and T. Sugiyama, J. Phys. Chem. Lett. **11**, 4422 (2020).
[22] C. Huygens, *Œuvres Complètes de Christiaan Huygens*, Vol. 15 (Nijhoff, The Hague, 1893).
[23] R. H. Dicke, Phys. Rev. **93**, 99 (1954).
[24] R. Bonifacio and L. A. Lugiato, Phys. Rev. A **11**, 1507 (1975).
[25] G. Timothy Noe II, J.-H. Kim, J. Lee, Y. Wang, A. K. Wójcik, S. A. McGill, D. H. Reitze, A. A. Belyanin, and J. Kono, Nat. Phys. **8**, 219 (2012).
[26] J. R. Harries, H. Iwayama, S. Kuma, M. Iizawa, N. Suzuki, Y. Azuma, I. Inoue, S. Owada, T. Togashi, K. Tono, M. Yabashi, and E. Shigemasa, Phys. Rev. Lett. **121**, 263201 (2018).
[27] G. Rainò, M. A. Becker, M. I. Bodnarchuk, R. F. Mahrt, M. V. Kovalenko, and T. Stöferle, Nature (London) **563**, 671 (2018).
[28] H. Varguet, S. Guérin, H. Jauslin, and G. Colas des Francs, Phys. Rev. B **100**, 041115(R) (2019).
[29] Y.-X. Zhang, Y. Zhang, and K. Mølmer, ACS Photonics **6**, 871 (2019).
[30] L. Mercadier, A. Benediktovitch, C. Weninger, M. A. Blessenohl, S. Bernitt, H. Bekker, S. Dobrodey, A. Sanchez-Gonzalez, B. Erk, C. Bomme, R. Boll, Z. Yin, V. P. Majety, R. Steinbrügge, M. A. Khalal, F. Penent, J. Palaudoux, P. Lablanquie, A. Rudenko, D. Rolles *et al.*, Phys. Rev. Lett. **123**, 023201 (2019).
[31] C. Zhou, Y. Zhong, H. Dong, W. Zheng, J. Tan, Q. Jie, A. Pan, L. Zhang, and W. Xie, Nat. Commun. **11**, 329 (2020).
[32] G. Findik, M. Biliroglu, D. Seyitliyev, J. Mendes, A. Barrette, H. Ardekani, L. Lei, Q. Dong, F. So, and K. Gundogdu, Nat. Photonics **15**, 676 (2021).
[33] I. Cherniukh, G. Rainò, T. Stöferle, M. Burian, A. Travesset, D. Naumenko, H. Amenitsch, R. Erni, R. F. Mahrt, M. I. Bodnarchuk, and M. V. Kovalenko, Nature (London) **593**, 535 (2021).
[34] N. Yokoshi, K. Odagiri, A. Ishikawa, and H. Ishihara, Phys. Rev. Lett. **118**, 203601 (2017).
[35] A. Ishikawa, K. Miyajima, M. Ashida, T. Itoh, and H. Ishihara, J. Phys. Soc. Jpn. **85**, 034703 (2016).
[36] M. Hoshina, N. Yokoshi, H. Okamoto, and H. Ishihara, ACS Photonics **5**, 318 (2018).
[37] E. M. Purcell and C. R. Pennypacker, Astrophys. J. **186**, 705 (1973).
[38] K. Ueno, J. Yang, Q. Sun, D. Aoyo, H. Yu, T. Oshikiri, A. Kubo, Y. Matsuo, Q. Gong, and H. Misawa, Appl. Mater. Today **14**, 159 (2019).
[39] K. Miyajima, Y. Kagotani, S. Saito, M. Ashida, and T. Itoh, J. Phys.: Condens. Matter **21**, 195802 (2009).
[40] M. Schuurmans, Opt. Commun. **34**, 185 (1980).
[41] E. M. Purcell, Phys. Rev. **69**, 681 (1946).
[42] Y. Sang, J. Han, T. Zhao, P. Duan, and M. Liu, Adv. Mater. **32**, 1900110 (2020).
[43] M. Gross and S. Haroche, Phys. Rep. **93**, 301 (1982).
[44] P. B. Johnson and R. W. Christy, Phys. Rev. B **6**, 4370 (1972).